HP-MULTIGRID FOR RANS-MODELED TURBULENT FLOWS IN A HIGH-ORDER FLUX RECONSTRUCTION FRAMEWORK

SAUMITRA JOSHI[1,2], AURELIO HURTADO DE MENDOZA[1,2], JIAQING KOU[1,2], KUNAL PURI[1], CHARLES HIRSCH[1] AND ESTEBAN FERRER[2]

[1] NUMECA International S.A.
189 Chaussee de la Hulpe, 1170 Bruxelles

[2] ETSIAE, Universidad Politécnica de Madrid
Plaza de Cardenal Cisneros 3, 28040 Madrid, Spain

Key words: High-order methods, Flux reconstruction, hp-multigrid, RANS, Spalart-Allmaras model

Abstract. High-order (HO) methods are of concerted academic and industrial interest in recent years due to their improved accuracy and their capability to deal with complex geometries [1]. Of particular note is the flux reconstruction method [2], which unifies several existing HO schemes into a simpler and computationally efficient approach that has been shown to work on all element types (including simplices) in two and three dimensions. There is considerable interest to apply HO methods to industrially relevant problems. At the same time, accurate and robust turbulence modeling techniques are essential for reliable results. As outlined in the National Aeronautics and Space Administration's CFD vision 2030 study, Large Eddy Simulation (LES) still remains impractical for industrial cases - therefore, Reynolds-Averaged Navier Stokes (RANS) and hybrid RANS-LES methods hold high significance in the near future [4].

Achieving fastest convergence to steady-state is important in the context of RANS simulations, for which several convergence acceleration techniques are being investigated. Multigrid methods are an industry standard in Finite Volume (FV) type schemes and are increasingly being applied to HO methods in the form of *p*-multigrid [22]. They exploit the polynomial hierarchy of the solution space to represent errors on a coarser resolution. A natural extension of this idea is *hp*-multigrid, where we can augument the classical *h*-multigrid to the polynomial hierarchy [23].

In this paper we illustrate the application of high-order flux reconstruction methods to simulate compressible, turbulent flows on body-fitted meshes. The case in point is the turbulent flow over a flat plate [24]. Turbulence is modeled through the RANS approach using the one-equation Spalart-Allmaras model. Grid-coarsening for the *h*-levels is performed by removing every other line in each direction from the original mesh. The system is driven to a steady-state solution using *hp*-multigrid convergence acceleration with local time-stepping using an explicit Runge-Kutta time-marcher. We show that the augumented *h*-multigrid is highly effective with a 10X to 24X drop in convergence time.

1 INTRODUCTION

Computational fluid dynamics (CFD) has come to be recognized as an indispensable tool in almost all branches of industrial design. Most industrially relevant flows are in the turbulent regime [3]. The scaling of computational cost at high Reynolds numbers makes (Direct Numerical Simulation) DNS infeasible for the foreseeable future. Consequently, focusing on the time-averaged behavior leads to the Reynolds-averaged Navier-Stokes (RANS) approach which is the industry-norm for turbulence modeling today [3]. RANS inherently smears out details in flow that would have been described by fluctuations at various length-scales and even results in inaccurate flow-behavior, e.g. for massively separated flows [6]. Large-eddy Simulation (LES) offers a compromise between DNS and RANS by resolving eddies greater than a cut-off width, while those with lesser size are modeled. Although grid requirements are significantly reduced compared to DNS, correct prediction of near-wall behavior using LES is still computationally intensive ($N_c \propto \mathrm{Re}^{\frac{13}{7}}$). Hybrid RANS-LES methods look to further reduce computational cost through coarser grids and increased modeling in near-wall regions. Nevertheless, there are several challenges that need to be overcome before LES and hybrid RANS-LES methods achieve industrial robustness, particularly their sensitivity to mesh distribution and parameter settings [5, 6, 7].

An orthogonal and complementary approach to reducing computational costs is to increase the accuracy delivered per degree-of-freedom. The current industrial workhorses are based on second-order accurate finite volume (FV) methods [3]. In comparison, "high-order" (HO) methods offer much higher accuracy per degree-of-freedom. Among the family of HO methods the discontinuous Galerkin (DG) method is by far the most dominant. More recently, Huynh [2] proposed the flux reconstruction (FR) method. A combination of these HO-methods with RANS and eventually hybrid RANS-LES techniques for turbulence modeling shows promise of making flows of higher Reynolds numbers viable.

Both steady-state and transient simulations are of importance in CFD. Transient flows can be treated as a sequence of steady-state simulations with timesteps comparable to the timescales of interest. Thus, developing efficient steady-state solvers is a widely researched topic. The defining characteristic of a good steady-state solver is a small time-to-convergence, and multigrid methods are widely used to minimize it [8, 9]. Since time-accuracy is irrelevant for steady-state simulations, cell-local time-stepping ensures the maximum possible timestep in each cell respecting local stability limits. Traditional multigrid methods are based on successively coarser meshes formed by agglomerating cells from finer meshes. We henceforth refer to them as h-multigrid. In HO-methods, alternatively to mesh-coarsening, we can represent the high-order errors on lower orders, effectively coarsening the polynomial-order p. The resulting p-multigrid has been extensively used for the last decade for elliptic, Euler and compressible Navier-Stokes equations [10, 11, 12, 13], including RANS. Pure h-multigrid has also been used in HO-methods for Navier-Stokes equations [15, 16, 14]. For turbulent flows, there are several studies that use h-multigrid and p-multigrid separately [18, 19]. To extract the most benefit out of multigrid in the context of HO-methods, a combination of h- and p-multigrid is a lucrative option. Indeed, several studies have explored the so-called hp-multigrid for compressible laminar flows [20, 21] and have successfully demonstrated h- and p-independence of convergence. Recent work by Fehn et al [23] conducted a detailed analysis of using hp-multigrid for the Poisson equation in the context of pressure-based Navier-Stokes equations. However, to the best of the authors' knowledge there exists no published study of the behavior of combined hp-multigrid with RANS-modeled density-based turbulent flows, which is the focus of this study.

2 GOVERNING EQUATIONS

We solve the compressible unsteady Navier-Stokes equations in conservative form with a Newtonian working fluid. The fluid viscosity is a function of temperature, and is modeled using Sutherland's law [25]. The modified Spalart-Allmaras (SA) turbulence model [26] is used to compute the eddy viscosity to ensure numerical stability in the presence of negative values of the turbulence variable ϑ, especially with coarse spatial discretization of the boundary layer edge. The governing equations are cast into the following compact form:

$$\partial_t \boldsymbol{U} + \partial_j (\boldsymbol{F}_{\text{ivc}} + \boldsymbol{F}_{\text{vsc}}) = \boldsymbol{S} \tag{1}$$

where $\boldsymbol{U} \in \mathbb{R}^{1 \times \mathcal{N}}$ is the solution-vector, $\boldsymbol{F}_{\text{ivc}} \in \mathbb{R}^{\mathcal{D} \times \mathcal{N}}$ and $\boldsymbol{F}_{\text{vsc}} \in \mathbb{R}^{\mathcal{D} \times \mathcal{N}}$ are the inviscid- and viscous-flux-vectors respectively, and $\boldsymbol{S} \in \mathbb{R}^{1 \times \mathcal{N}}$ is the source-term-vector. $\mathcal{N}$ is the number of solution-variables and $\mathcal{D}$ is the spatial dimension. These are defined as:

$$\boldsymbol{U} = \begin{bmatrix} \rho \\ \rho v_1 \\ \rho v_2 \\ \rho v_3 \\ \rho E \end{bmatrix} \quad , \quad \boldsymbol{F}_{\text{ivc}} = \begin{bmatrix} \rho v_1 & \rho v_2 & \rho v_3 \\ p + \rho v_1 v_1 & \rho v_1 v_2 & \rho v_1 v_3 \\ \rho v_2 v_1 & p + \rho v_2 v_2 & \rho v_2 v_3 \\ \rho v_3 v_1 & \rho v_3 v_2 & p + \rho v_3 v_3 \\ \rho v_1 H & \rho v_2 H & \rho v_3 H \end{bmatrix} \quad , \tag{2}$$

$$\boldsymbol{F}_{\text{vsc}} = \begin{bmatrix} 0 & 0 & 0 \\ \tau_{11} & \tau_{12} & \tau_{13} \\ \tau_{21} & \tau_{22} & \tau_{23} \\ \tau_{31} & \tau_{32} & \tau_{33} \\ v_i \tau_{i1} + \omega_1 & v_i \tau_{i2} + \omega_2 & v_i \tau_{i3} + \omega_3 \end{bmatrix} \quad , \quad \boldsymbol{S} = \begin{bmatrix} 0 \\ 0 \\ 0 \\ 0 \\ 0 \end{bmatrix} .$$

Einstein summation convention is used for repeated indices i. The symbols used in the equations above are: ρ is the density, $\boldsymbol{v} = \boldsymbol{e}_i v_i$ is the velocity vector with $\boldsymbol{e}_i$ being the i-th orthonormal basis vector of Euclidean space, E is the total energy per unit mass, i.e. $E = e + \frac{1}{2} v_i v_i$ where e is the internal energy. For a calorically perfect gas, $e = \frac{RT}{\gamma - 1}$ where R is the gas constant and T is the temperature determined as $T = \gamma M^2 p / \rho$. The total enthalpy H is defined as $H = E + \frac{p}{\rho}$ where p is the pressure, related to energy through the ideal gas law:

$$p = \rho (\gamma - 1) \left(E - \frac{1}{2} v_i v_i \right)$$

where γ is the specific heat ratio. τ_{ij} are the components of the viscous stress tensor $\underline{\underline{\tau}}$. For compressible Newtonian fluids:

$$\tau_{ij} = 2\mu S_{ij} \quad , \quad S_{ij} = \frac{1}{2} \left(\partial_i v_j + \partial_j v_i \right) - \frac{1}{3} \partial_k v_k \delta_{ij}$$

3

where μ is the dynamic viscosity which is assumed to be constant. $\omega_j = \lambda \partial_j T$ is the j-th component of the heat flux vector where $\lambda = \frac{\gamma R}{\gamma - 1} \frac{\mu}{\text{Pr}}$ is the molecular conductivity. Unless specified otherwise, the laminar Prandtl number $\text{Pr} = 0.72$.

For the SA model, the eddy viscosity μ_t is calculated from the turbulence variable ϑ and the kinematic viscosity ν as

$$\mu_t = \begin{cases} \rho \vartheta f_{v_1} & \text{if } \vartheta \geqslant 0 \\ 0 & \text{otherwise} \end{cases} \quad , \quad f_{v_1} = \frac{\chi^3}{\chi^3 + c_{v_1}^3} \quad , \quad \chi = \vartheta/\nu \quad , \quad c_{v_1} = 7.1. \tag{3}$$

To ensure positivity and C^1-continuity of the diffusion coefficient it is defined as

$$\eta = \begin{cases} \mu(1 + \chi) & \text{if } \vartheta \geqslant 0 \\ \mu\left(1 + \chi + \frac{1}{2}\chi^2\right) & \text{otherwise.} \end{cases} \tag{4}$$

The production term $\mathcal{G}$ is defined as

$$\mathcal{G} = \begin{cases} c_{b_1} \tilde{s} \rho \vartheta & \text{if } \vartheta \geqslant 0 \\ c_{b_1} s \rho \vartheta g_n & \text{otherwise} \end{cases} \quad , \quad c_{b_1} = 0.1355 \quad , \quad g_n = 1 - \frac{1000\chi^2}{1 + \chi^2}. \tag{5}$$

$s = \left|\varepsilon_{ijk} \partial_j v_k\right|$ is the vorticity magnitude with ε_{ijk} being the Levi-Civita symbol for permutation. $\tilde{s}$ is the modified vorticity defined as

$$\tilde{s} = \begin{cases} s + \bar{s} & \text{if } \bar{s} \geqslant -c_{v_2} s \\ s + \dfrac{s\left(c_{v_2}^2 s + c_{v_3} \bar{s}\right)}{(c_{v_3} - 2c_{v_2})s - \bar{s}} & \text{otherwise} \end{cases} \quad , \quad \bar{s} = \frac{\vartheta f_{v_2}}{\kappa^2 d_w^2} \tag{6}$$

$$f_{v_2} = 1 - \frac{\chi}{1 + \chi f_{v_1}} \quad , \quad c_{v_2} = 0.7 \quad , \quad c_{v_3} = 0.9 \quad , \quad \kappa = 0.41$$

with d_w being the distance to the nearest wall. Note the difference between $\tilde{s}$ and $\bar{s}$. The destruction term $\mathcal{Y}$ is defined as

$$\mathcal{Y} = \begin{cases} c_{w_1} f_w \dfrac{\rho \vartheta^2}{d_w^2} & \text{if } \vartheta \geqslant 0 \\ -c_{w_1} \dfrac{\rho \vartheta^2}{d_w^2} & \text{otherwise} \end{cases} \tag{7}$$

with the terms having the following definition:

$$c_{w_1} = \frac{c_{b_1}}{\kappa^2} + \frac{1 + c_{b_2}}{\sigma} \tag{8}$$

$$f_w = g \left(\frac{1 + c_{w_3}^6}{g^6 + c_{w_3}^6} \right)^{\frac{1}{6}} \quad , \quad g = r + c_{w_2} \left(r^6 - r \right) \quad , \quad r = \min \left(\frac{\vartheta}{\tilde{s} \kappa^2 d_w^2} \, , \, r_{\max} \right)$$

$$r_{\max} = 2 \quad , \quad c_{b_2} = 0.622 \quad , \quad c_{w_2} = 0.3 \quad , \quad c_{w_3} = 2 \quad , \quad \sigma = \frac{2}{3}.$$

The trip term $\mathcal{T}$ is set to 0 throughout this work as we are concerned with flows in the fully turbulent regime. The term $\mathcal{K}$ is defined as

$$\mathcal{K} = \frac{c_{b_2}}{\sigma} \rho \partial_j \vartheta \partial_j \vartheta. \tag{9}$$

3 FLUX RECONSTRUCTION METHOD

The physical space $\Omega \in \mathbb{R}^{\mathcal{D}}$ is discretized into N_c distinct cells. In each, the solution is represented by a Lagrange polynomial of order p at $(p+1)^{\mathcal{D}}$ Gauss-solution-points. This solution is cell-wise-discontinuous. The flux-reconstruction method [2] constructs a semi-discrete form of (1) as

$$\partial_t \boldsymbol{U} = -\nabla^\delta \cdot \left(I^{p+1}_{\boldsymbol{F}_{\mathrm{ivc}} \delta C} + I^{p+1}_{\boldsymbol{F}_{\mathrm{vsc}} \delta C} \right) + \boldsymbol{S}^\delta \tag{10}$$

where $I^{p+1}_{\boldsymbol{F}_{\mathrm{ivc}} \delta C}$ and $I^{p+1}_{\boldsymbol{F}_{\mathrm{vsc}} \delta C}$ are piecewise C^0-continuous inviscid and viscous fluxes respectively. These are constructed from the discontinuous fluxes

$$\begin{aligned}
\boldsymbol{F}_{\mathrm{ivc}}{}^\delta &= \boldsymbol{F}_{\mathrm{ivc}} \left(\boldsymbol{U}^\delta \right) \\
\boldsymbol{F}_{\mathrm{vsc}}{}^\delta &= \boldsymbol{F}_{\mathrm{vsc}} \left(\boldsymbol{U}^\delta, \boldsymbol{Q}^\delta \right).
\end{aligned} \tag{11}$$

to which corrections are added to ensure that they are continuous at cell-interfaces. The interface-values are calculated using Riemann solvers borrowed from the finite-volume world as

$$\begin{aligned}
\boldsymbol{F}_{\mathrm{ivc}}{}^{\delta I} &= \mathcal{R}_{\boldsymbol{F}_{\mathrm{ivc}}} \left(\boldsymbol{U}_-^{\delta F}, \boldsymbol{U}_+^{\delta F} \right) \\
\boldsymbol{F}_{\mathrm{vsc}}{}^{\delta I} &= \mathcal{R}_{\boldsymbol{F}_{\mathrm{vsc}}} \left(\boldsymbol{U}_-^{\delta F}, \boldsymbol{Q}_-^{\delta F}, \boldsymbol{U}_+^{\delta F}, \boldsymbol{Q}_+^{\delta F} \right).
\end{aligned} \tag{12}$$

where $\boldsymbol{U}_-^{\delta F}$ and $\boldsymbol{U}_+^{\delta F}$ are the discontinuous solution-values interpolated to the interface from the left and right respectively. Likewise, $\boldsymbol{Q}_-^{\delta F}$ and $\boldsymbol{Q}_+^{\delta F}$ are the interpolated discontinuous corrected gradients. We use the Roe solver for the inviscid flux and the local discontinuous-Galerkin (LDG) solver for the viscous flux. For a detailed description, the reader is referred to [28].
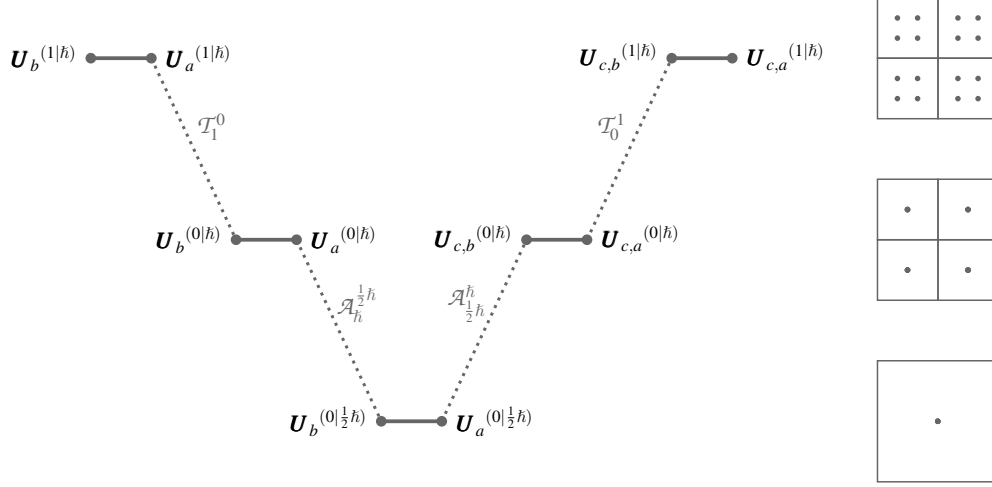
4 *HP*-MULTIGRID

Figure 1: Schematic depiction of one V-cycle of the *hp*-multigrid algorithm. Solid lines represent smoothing, dashed lines represent restriction and prolongation. On the right is a representation of the degrees of freedom at every level.

The semi-discrete form of (10) is accelerated to steady state using combined *h*- and *p*-multigrid Full Approximation Scheme (FAS). Figure 1 depicts one V-cycle. A recently developed Runge-Kutta-54 scheme with optimized coefficients [29] is used as a smoother. This scheme allows us to take larger timesteps without affecting stability, at a cost of loss in time-accuracy which is not of concern to when seeking steady-state solutions. Restriction on the *p*-levels ($\mathcal{T}_1^0$ in figure) is performed using an $\mathbb{L}^2$ projection, and on the *h*-levels ($\mathcal{A}_\hbar^{\frac{1}{2}\hbar}$ in figure) using weighted averaging of fine-grid values. Conversely, prolongation of the correction on *h*-levels ($\mathcal{A}_{\frac{1}{2}\hbar}^\hbar$ in figure) for every coarse unified cell simply sets its value to all the agglomerated cells that constitute it. Prolongation on *p*-levels is done using an $\mathbb{L}^2$ projection.

Since we are interested in the steady-state solution, time-accuracy is not important. We therefore can take as large a timestep as permissible by stability limits, which can vary from cell-to-cell. For a given cell C_i, with Δx_i being the shortest distance between two solution-points in that cell and CFL being the appropriately selected Courant-Friedrich-Lewy number, the local time-step is

$$\Delta t_i = \text{CFL} \cdot \frac{\Delta x_i}{\left(\|\boldsymbol{v}_i\| + \frac{\gamma p_i}{\rho_i}\right) + \left(\frac{\nu_i + \frac{\mu_{ti}}{\rho_i}}{\Delta x_i}\right)}. \tag{13}$$

5 VERIFICATION: MANUFACTURED SOLUTIONS

We use the method of manufactured solutions to verify the correctness of the implementation. The manufactured solution proposed in [30] is used, which mimics a realistic near-wall turbulent flow pattern.
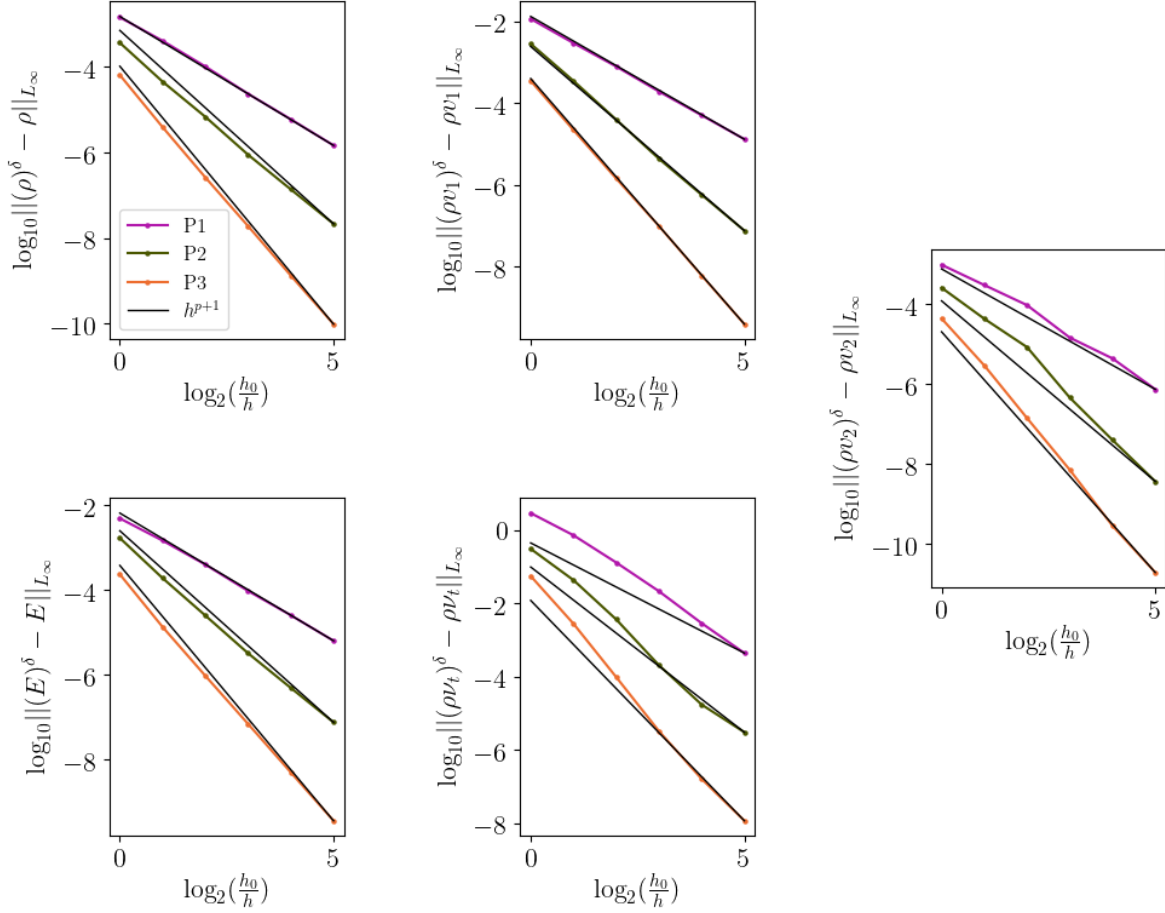
Figure 2: hp-convergence for MMS for all five flow-variables compared against the expected drop in error of h^{p+1}. The abscissa represents increasingly finer mesh-resolution. We observe that, with sufficiently finer meshes, all orders eventually align with the expected rate of h^{p+1}.
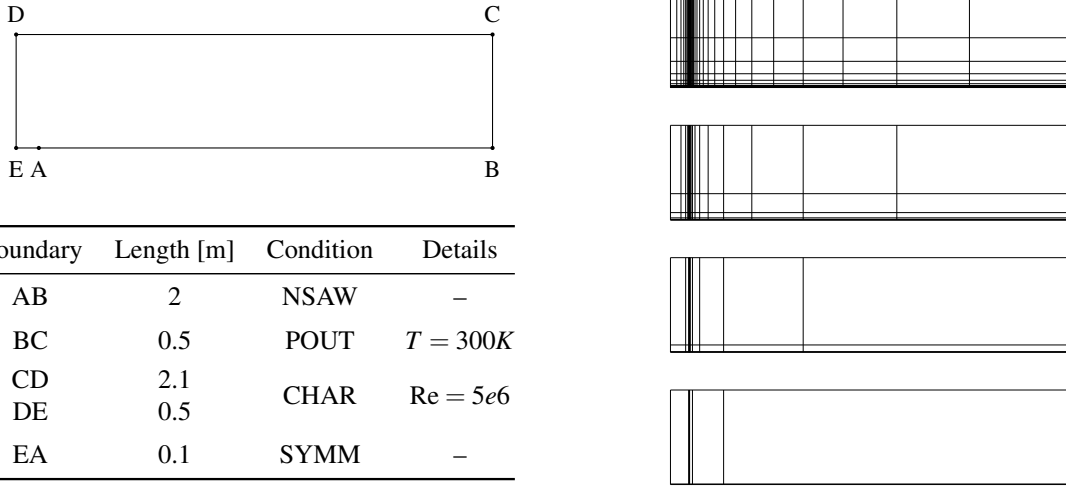
In particular, the correctness of the implementation for the no-slip adiabatic wall boundary condition is verified, which is essential for accurate prediction of physical quantities of interest in aerodynamic flows, such as lift and drag. The analysis is done for $p \in [1,3]$ and a hierarchy of six grids in h. All runs are converged to an absolute $\mathbb{L}^2$ residual norm of 10^{-8}. Figure 2 shows the drop in L_∞-error of all flow-variables with increasing h and p. With sufficient refinement, the error for all flow-variables attains the expected drop rate of h^{p+1}, verifying the correctness of the implementation.

6   RESULTS

The case under consideration is turbulent flow over a flat-plate [31] at Reof $5,000,000$ and Mach 0.2. The plate is 2 meters long and is modeled as a no-slip adiabatic wall. The left and top boundaries are treated as non-reflective openings with flow entering from the left. The right boundary is a pressure outlet with a fixed temperature of 300 Kelvin. A distance of 0.1 meters before the plate is left to avoid

Table 1: Schematic diagram of the simulation domain and boundary-conditions for turbulent flow over a flat-plate. On the right is the hierarchy of h-meshes used in hp-multigrid for the turbulent flat-plate case. The top-most mesh in is the original mesh. Each subsequent mesh in the hierarchy is created by removing every other mesh-line in each direction, reducing the number of cells by a factor of 4 each time. The number of cells in the original mesh is 768. The x_2^+ of the first near-wall cell for the original mesh is 4.

Boundary	Length [m]	Condition	Details
AB	2	NSAW	–
BC	0.5	POUT	$T = 300K$
CD	2.1	CHAR	$Re = 5e6$
DE	0.5		
EA	0.1	SYMM	–

influence of the inlet and is modeled as a reflective wall. A schematic is shown in Table 1 along with the meshes.

We run simulations from P2 to P5 using both p-multigrid and hp-multigrid for acceleration to steady-state. The variables are initialized to constant freestream values. The CFL for all runs lies between 0.5 and 1, and a geometric sweep-pattern is used on the V-cycles. Simulations are run until a drop of 5 orders of magnitude in residual-norm. Several physical quantities of interest are monitored for all runs. These are:

- Skin-friction coefficient C_f along the wall,
- Time-history of C_f at a distance of 0.97008 m from the leading-edge (henceforth Position-X),
- Time-history of drag-coefficient C_d along the entire plate,
- Profiles of wall-normalized x-velocity v_1^+ in the x_2 direction at Position-X and at a distance of 1.90334 m from the leading-edge (henceforth Position-Y), and
- Profiles of turbulence variable ϑ in the x_2 direction at Position-X.

We observe in Figure 3 that hp-multigrid outperforms p-multigrid at the damping out of low frequency errors, showing a significant reduction of the number of V-cycles by a factor of 10 to 24. Note that the apparent improvement in convergence of p-multigrid from P2 to P5 is because as we increase the P5 there are a greater number of sweeps performed on the coarser grid. C_f and C_d converge in less than 15000 V-cycles for all polynomial orders. For P4 and P5 the error in drag is less than 1 count, and the error in C_f is less than 1%. The spatial distribution of different quantities of interest also agrees well with the expected values from reference data.
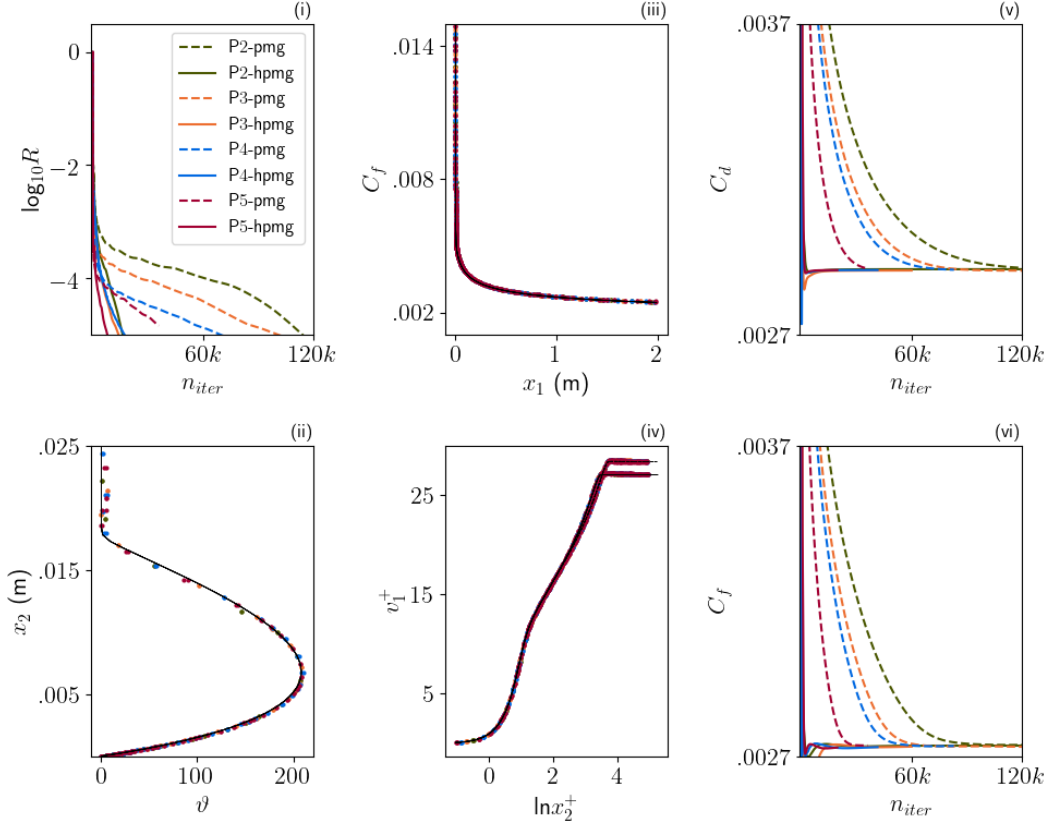
8

Figure 3: *p*-multigrid versus *hp*-multigrid. Comparison of residual evolution (i), wall-normal variation of ϑ at Position-X (ii), C_f along plate (iii), wall-normal variation of v_2 at Position-X and Position-Y (iv), with reference data (solid lines). Comparison evolution of C_d (v) and of C_f at Position-X (vi). We observe a clear reduction in the number of V-cycles necessary for convergence in *hp*-multigrid as compared to *p*-multigrid, in this case by a factor of 10 to 24. At the same time, the results agree well with reference data.

7 OUTLOOK

In this study we have demonstrated the superiority of *hp*-multigrid over *p*-multigrid for acceleration to steady-state of RANS-modeled turbulent flow over a flatplate. Our future work focuses on extending *hp*-multigrid to steady-state RANS flow scenarios in 2D and 3D with the overarching objective of applying the technique to pseudo-steady-state convergence for transient flows using dual-timestepping.

REFERENCES

[1] Huynh, H. T., Wang, Z. J., Vincent, P. E. High-order methods for computational fluid dynamics: a brief review of compact differential formulations on unstructured grids. *Computers & Fluids* (2014) 98:209–220.

[2] Huynh, H.T.: A flux reconstruction approach to high-order schemes including discontinuous Galerkin methods. AIAA Computational Fluid Dynamics Meeting (2007).

[3] Slotnick, J. et al: CFD vision 2030 study: A path to revolutionary computational aerosciences (2014)

[4] Slotnick, J., Khodadoust, A., Alonso, J., Darmofal, D., Gropp, W., Lurie, E., Mavriplis, D.: CFD vision 2030 study: A path to revolutionary computational aerosciences. NASA Technical Report, NASA/CR-2014-218178, NF1676L-18332 (2014)

[5] Bose, S.T. and Park, G.I.: Wall-modeled large-eddy simulation for complex turbulent flows, Ann. Review. of Fluid Mech. (2018)

[6] Heinz, S.: A review of hybrid RANS-LES methods for turbulent flows: concepts and applications, Progress in Aero. Sci. (2020)

[7] Ekman, P. et. al.: Assessment of hybrid RANS-LES methods for accurate automotive aerodynamic simulations, J. Wind. Engg. and Indus. Aero. (2020)

[8] Wesseling, P. and Oosterlee, C.W.: Geometric multigrid with applications to computational fluid dynamics, J. Comp. and Applied. Math. (2001)

[9] Stüben, K.: A review of algebraic multigrid, J. Comp. and Applied. Math. (2001)

[10] Haga, T. et. al.: Efficient solution techniques for high-order methods on 3D anisotropic hybrid meshes, AIAA Aerospace Science Meet (2011)

[11] Luo, H. et. al.: An implicit discontinuous Galerkin method for the unsteady compressible Navier–Stokes equations, Computers Fluids (2012)

[12] Ghidoni, A. et. al.: Efficient p-multigrid discontinuous Galerkin solver for complex viscous flows on stretched grids, Int. J. for Num. Methods in Fluids (2014)

[13] Franciolini, M. et. al.: p-Multigrid matrix-free discontinuous Galerkin solution strategies for the under-resolved simulation of incompressible turbulent flows, Computers Fluids (2020)

[14] Fehn, N. et. al.: Efficiency of high-performance discontinuous Galerkin spectral element methods for under-resolved turbulent incompressible flows, Int. J. for Num. Methods in Fluids (2018)

[15] Botti, L. et. al.: h-multigrid agglomeration based solution strategies for discontinuous Galerkin discretizations of incompressible flow problems, J. Comp. Phy. (2017)

[16] Krank, B. et. al.: A high-order semi-explicit discontinuous Galerkin solver for 3D incompressible flow with application to DNS and LES of turbulent channel flow, J. Comp. Phy. (2017)

[17] Fehn, N. et. al.: Hybrid multigrid methods for high-order discontinuous Galerkin discretizations, J. Comp. Phy. (2020)

[18] Wallraff, M. and Leicht, T.: Higher order multigrid algorithms for a discontinuous Galerkin RANS solver, AIAA SciTech (2014)

[19] Wallraff, M. et. al., Multigrid solver algorithms for DG methods and applications to aerodynamic flows, IDIHOM, Springer (2015)

[20] Nastase, C.R. and Mavriplis, D.J.: High-order discontinuous Galerkin methods using an hp-multigrid approach, J. Comp. Phy. (2006)

[21] Shahbazi, K., et. al.: Multigrid algorithms for high-order discontinuous Galerkin discretizations of

the compressible Navier–Stokes equations, J. Comp. Phy. (2009)

[22] Rueda-Ramírez, A.M., Manzanero, J., Ferrer, E., Rubio, G., Valero, E.: A p-multigrid strategy with anisotropic p-adaptation based on truncation errors for high-order discontinuous Galerkin methods. *Journal of Computational Physics* (2019)

[23] Fehn, N. et. al.: Hybrid multigrid methods for high-order discontinuous Galerkin discretizations. *Journal of Computational Physics* (2020)

[24] Langley Research Center, Turbulence Modeling Resource: 2D turbulent flow over flat-plate `https://turbmodels.larc.nasa.gov/flatplate_sa.html`

[25] Schlichting, H.: Boundary Layer Theory, McGraw-Hill (1979)

[26] Oliver, T.A.: A high-order, adaptive, discontinuous Galerkin finite element method for the Reynolds-Averaged Navier-Stokes equations. MIT, Cambridge, Dept. of Aeronautics and Astronautics (2008)

[27] Advanced High-Order Simulation Methods for Industrial Applications. `https://cordis.europa.eu/project/id/813605`

[28] Castonguay, P.: High-order energy stable flux reconstruction schemes for fluid flow simulations on unstructured grids, Ph.D. thesis, Stanford University (2012)

[29] Vermeire, B.C. et. al.: Optimal Runge–Kutta schemes for pseudo time-stepping with high-order unstructured methods, J. Comp. Phy. (2019)

[30] Navah, F., Nadarajah, S.: On the verification of CFD solvers of all orders of accuracy on curved wall-bounded domains and for realistic RANS flows, Computers and Fluids (2020)

[31] `https://turbmodels.larc.nasa.gov/flatplate_sa.html` (last accessed 25.02.2021)